WILEY-VCH

Efficient Gate-tunable Hot-carrier Photocurrent from Perovskite Multiple Quantum Wells

Chenhao Wang, Qi Wei, Hui Ren, Kin Long Wong, Qi Liu, Luwei Zhou, Pengzhi Wang, Songhua Cai, Jun Yin, Mingjie Li**

Dr. C. Wang, Dr. Q. Wei, Hui Ren, Kin Long Wong, Qi Liu, Luwei Zhou, Dr. P. Wang, Prof. S. Cai, Prof. J. Yin, Prof. M. Li

Department of Applied Physics, The Hong Kong Polytechnic University, Hung Hom, Kowloon, Hong Kong, China

Prof. M. Li

Shenzhen Research Institute, The Hong Kong Polytechnic University, Shenzhen, Guangdong, 518057, China

Photonics Research Institute, The Hong Kong Polytechnic University, Hung Hom, Kowloon, Hong Kong, China

Corresponding Author Email:
ming-jie.li@polyu.edu.hk (Prof. Mingjie Li); jun.yin@polyu.edu.hk (Prof. J. Yin)

Keywords: Perovskite multiple Quantum wells, 2D heterostructure, MoS_2, Hot carrier extraction, Hot carrier photocurrent

Abstract

Hot-carrier relaxation above the bandgap results in significant energy losses, making the extraction of hot carriers a critical challenge for efficient hot-carrier photocurrent generation in devices. In this study, we observe long-lived hot carriers in the metal-halide perovskite multiple quantum wells, $(BA)_2(MA)_{n-1}Pb_nI_{3n+1}$ (n=3), and demonstrate effective hot-hole photocurrent generation using 2D MoS_2 as an extraction layer. We achieve a high external quantum efficiency of short-circuit hot-carrier photocurrent of up to 35.4%. Further enhancement in photocurrent efficiency and open-circuit photovoltage is observed when a gate electric field is applied, resulting in an external quantum efficiency of up to 61.9%. Evidence of hot-hole extraction is validated through operando transient reflection measurements on the working devices, with studies that depend on wavelength, carrier density, and gate voltage. DFT calculations on the heterostructure devices under different bias voltages further elucidate the mechanism of hot-hole extraction enhancement. These findings underscore the potential of perovskite multiple quantum wells as long-lived hot-carrier generators and highlight the role of 2D transition metal dichalcogenide semiconductors as efficient hot-carrier extraction electrodes for low-power optoelectronics.

1. Introduction

Hot carriers (HCs) generated above the semiconductor band edge relax rapidly through interactions with phonons, resulting in significant energy losses.[1-5] Efficient utilization of hot carriers for the photon-to-current conversion has the potential to enhance the power conversion efficiency and exceed the Shockley-Queisser limit.[3, 6] [7-10] Various device structures and materials have been explored to harness HCs for hot-carrier photocurrent and photovoltage generation, including nanomaterials such as plasmonic Au nanoparticles,[11-13] III-V group quantum wells,[14] nanowire nanoantennas.[15] However, efficient hot-carrier photocurrent generation has been rarely achieved, with reported efficiencies of ~1% or lower. The low external quantum efficiency (EQE) is mainly due to the fast HC relaxation in metal and conventional semiconductor materials.[15-17] While efficient hot-carrier extraction (up to ~80%) has been demonstrated using the ultrafast optical spectroscopy[16-19] in the low-dimensional heterostructures such as perovskite quantum dots/organic films,[19] 2D material heterostructures,[18] the HC photocurrent based on these materials has not yet been reported. Therefore, advancing hot-carrier devices using low-dimensional semiconductor heterostructures is essential.

Organic-inorganic hybrid perovskites have demonstrated excellent performance in solution-processed optoelectronics[20-22] and exhibit a reduced HC relaxation rate as compared to conventional materials.[17, 23-28] By reducing the inorganic layer of three-dimensional (3D) perovskite to fewer layers, quasi-two-dimensional (quasi-2D) Ruddlesden-Popper (RP) perovskite multiple quantum wells (MQWs) can be formed, following the formula $L_2A_{n-1}M_nX_{3n+1}$, where L represents a large organic cation, A is a short monovalent organic cation, M is Pb or Sn, X represents a halide, and *n* denotes the number of octahedral MX_6 MQWs layers between adjacent insulating organic layers.[29-31] Notably, perovskite MQWs with $3 \leq n < \infty$ exhibit both quantum confinement effect and reduced carrier-phonon coupling. This configuration can extend HC cooling through the phonon bottleneck effect, enhancing HC extraction.[17, 32] Compared with perovskite bulk polycrystalline films and their 3D and quantum dot (QDs) counterparts, MQW also allow

for controllable thickness tuning via mechanical exfoliation, enabling the production of multilayers in the range of 100 nm. This feature makes them particularly suitable for the HC transport and extraction.[33] Additionally, 2D perovskites provide improved optical and thermal stability,[20] making them ideal absorber layers for HC optoelectronic devices. However, whether and how hot carriers can be efficiently harvested in perovskite MQW devices remains an open question.

2D transition metal dichalcogenide (TMDC) materials are recognized for their high carrier mobility, tunable bandwidth, and excellent stability. This has led to significant interest in their application in emerging optoelectronic devices.[34-37] 2D TMDCs have also been utilized as charge-selective contacts in 2D Van der Waals (vdW) heterostructure devices, as well as in perovskite solar cells and photodetectors.[38-40] These properties make them promising candidates for HC extraction layer in perovskite MQW for efficient HC photocurrent generation.

Here, we develop a 2D vdW heterostructure HC-device that utilizes perovskite $(BA)_2(MA)_2Pb_3I_{10}$ MQWs as the light-absorbing layer and few-layer MoS_2 as the hot-hole extraction contact. Efficient hot-hole photocurrent from the perovskite to MoS_2, achieving EQE of up to 35.4% and 61.9% without and with the gate voltage, respectively, alongside an enhanced open-circuit voltage (V_{OC}) under short-wavelength photoexcitation. Operando transient-reflection spectroscopy measurements conducted on the working device provide clear evidence of hot carrier extraction and photocurrent generation. We also find that the hot-hole extraction can be further fine-tuned by adjusting the gate voltage, which influences the height of the extraction energy barrier in the heterostructure, as confirmed by density functional theory (DFT) calculations. These findings illustrate how to effectively harness hot carriers in devices, paving the way for advancing low-power optoelectronic applications.

2. Results and discussion

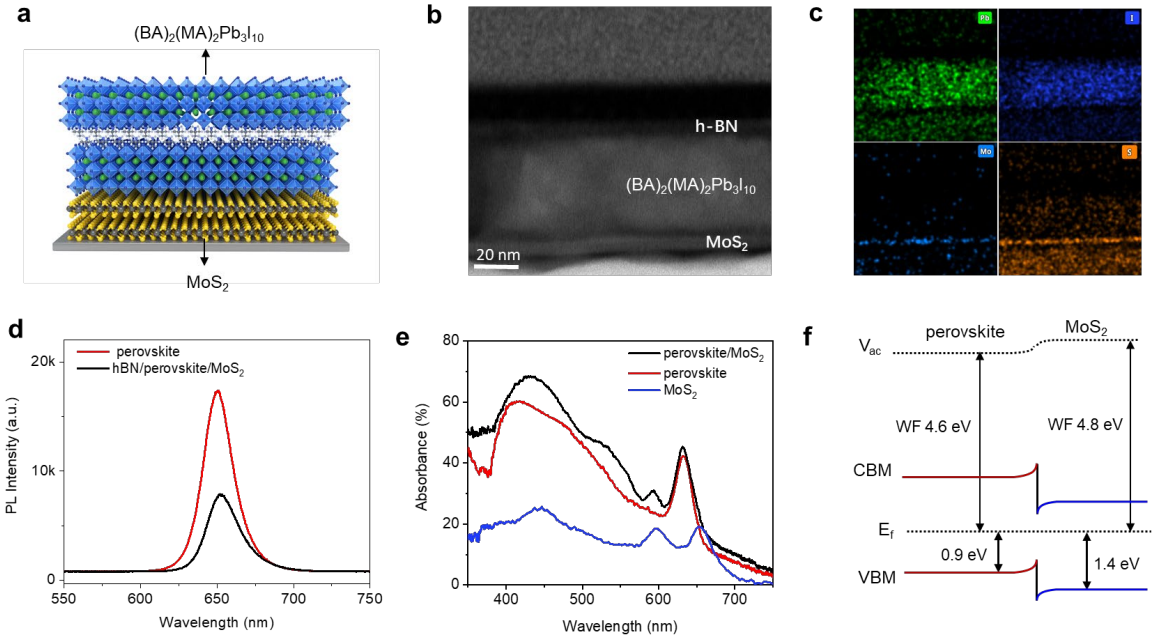

Figure 1. Structure and optical properties of the $(BA)_2(MA)_2Pb_3I_{10}$ perovskite/MoS_2 heterostructure. a) Schematic diagram of heterostructure. b-c) Cross-sectional TEM and EDS mapping images of the vertically stacked heterostructure. d) Photoluminescence spectra of $(BA)_2(MA)_2Pb_3I_{10}$ perovskite and the perovskite/MoS_2 heterostructure under illumination of λ_{exc} = 532 nm. e) Absorption spectra of MoS_2, perovskite and heterostructure. f) Energy level alignment of the heterostructure (V_{ac}=vacuum level, WF=work function, CBM=conduction band minimum, VBM=valence band maximum, E_f=Fermi level).

2.1. Structural and optical properties

$(BA)_2(MA)_2Pb_3I_{10}$ (n=3, BA: $C_4H_9NH_3$; MA: CH_3NH_3) perovskite layer was exfoliated from a single crystal prepared using a temperature-programmed solution method (see Figure S1 and XRD pattern in Figure S2, Supporting Information for details). The 2D perovskite/MoS_2 heterostructure (illustrated schematically in **Figure 1**a) was achieved using the dry transfer method. Figure 1b displays the cross-sectional transmission electron microscopy (TEM) image of the heterostructure, which is covered with an h-BN layer to prevent decomposition and contamination. The AFM image of heterostructure is also provided in Figure S3, Supporting Information. The thicknesses of MoS_2 and perovskite are ~ 5 nm and ~ 60 nm, respectively. Corresponding energy-dispersive X-ray spectroscopy

(EDS) mappings reveal a uniform composition distribution across the device (Figure 1c). Figure 1d presents the photoluminescence spectra of the perovskite, with a peak located at ~ 650 nm. The spectrum of the heterostructure shows reduced intensity due to the charge transfer from perovskite to MoS_2. Figure 1e illustrates the absorption (A) spectra derived from transmission (T) and reflection (R) spectra measurements, calculated using A=1 - R - T (additional details are provided in the Supporting Information). A sharp peak at ~ 630 nm in the perovskite indicates an exciton transition. The XRD peaks and exciton transition positions of perovskite, consistent with previous reports[41-42], confirm that n = 3 in our $(BA)_2(MA)_{n-1}Pb_nI_{3n+1}$. The MoS_2 layer exhibits three peaks at ~ 670, 600 and 430 nm, corresponding to the A-/B-/C-exciton transitions, respectively. The spectrum of the heterojunction closely resembles that of the perovskite, with a minor contribution from MoS_2, implying that the incident photons are primarily absorbed in the perovskite, given its significantly larger thickness and higher absorption coefficient.

To effectively extract hot carriers from the perovskite before they relax, the conduction band minimum of the extraction layer must be higher than that of the perovskite for hot-electron extraction, and the valence band maximum must be higher for hot-hole extraction. Ultraviolet photoemission spectroscopy (UPS) was employed to assess the energy level alignment of the heterostructure (see Figure 1f, and Figure S4 in the Supporting Information for details). The results indicate a valence band minimum (VBM) offset of 0.5 eV between MoS_2 and the perovskite, which acts as the hot-hole energy barrier (E_B). This result suggests that MoS_2 could effectively extract hot holes from the photoexcited perovskite, thereby facilitating the generation of hot-hole photocurrent.

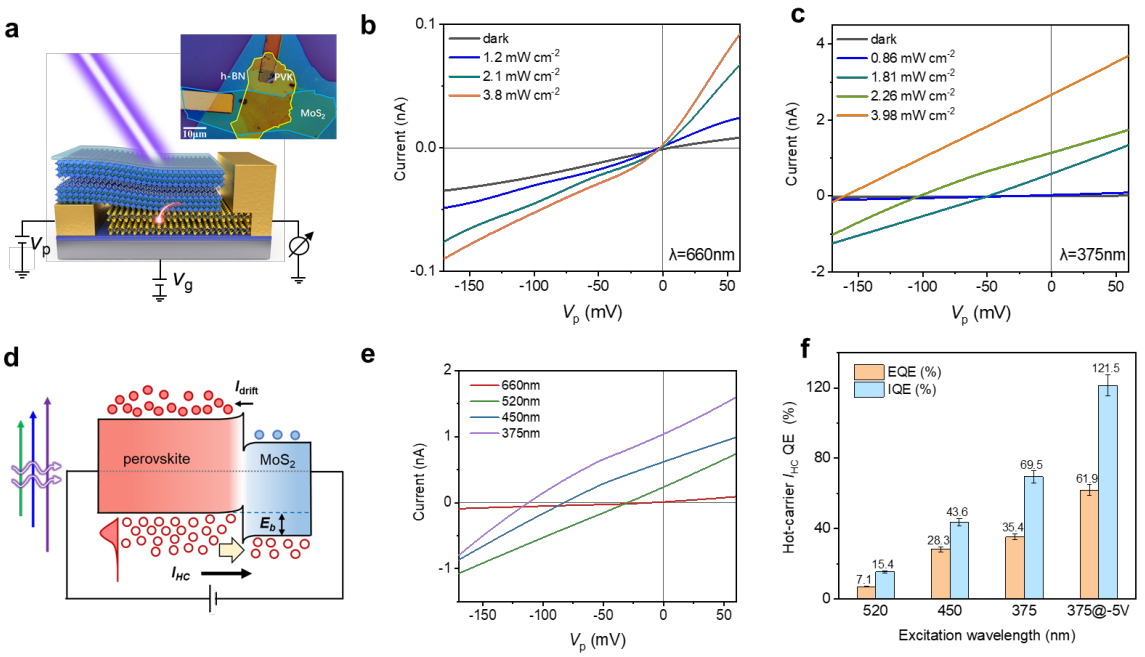

Figure 2. Hot-hole photocurrent and photovoltage of the heterostructure. a) Schematic diagram of the device under illumination where a hot hole is extracted from perovskite to MoS_2 with an optical image inset. I-V characteristics of the device under dark conditions and illumination of b) 660 nm and c) 375 nm with increased power density. d) Schematic band alignment and hot-hole transport of the device under illumination. e) I-V characteristics of the device under illumination with different wavelengths at a constant absorbed fluence of 9.08×10^9 photons s^{-1} in the active area of the heterostructure. f) Short-circuit hot-carrier photocurrent EQE and IQE of the device under illumination of 520 nm, 450 nm and 375 nm (with V_g of 0 and -5 V) obtained from (e).

2.2. Hot-hole photocurrent and photovoltage generation

To test the above hypothesis and investigate hot-hole photocurrent generation, a vertical 2D perovskite/MoS_2 heterostructure device was fabricated (see the schematic and optical images in **Figure 2**a; fabrication procedures are detailed in Figure S5, Supporting Information). In this device, the perovskite MQWs connect to the positive electrode, while MoS_2 connects to the negative electrode, facilitating hole current under forward bias. When carriers are injected under 660 nm excitation, the device exhibits typical PN junction characteristics, with almost no short-circuit photocurrent observed, even at high pump intensities (Figure 1b). In contrast, when hot carriers are generated in the perovskite under shorter wavelength excitation (e.g., 375 nm, 3.3 eV), the positive short-circuit photocurrent and photovoltaics effects are clearly observed (Figure 1c). Since the incident photons are

primarily absorbed by the perovskite, the positive short-circuit current is mainly driven by hole transport from the perovskite (connected to the positive electrode) to the MoS_2 (connected to the negative electrode). Despite the presence of a hole barrier (~ 0.5 eV), the net positive short-circuit photocurrent indicates that the hot-hole current (I_{HC}), generated by transport from perovskite to MoS_2, exceeds the drift current I_{drift}, which is the electron drift from perovskite to MoS_2 due to the interfacial electric field. The short-circuit photocurrent is also observed under 450 nm and 520 nm illumination (see Figure S6, Supporting Information, for details), along with higher photocurrents and open-circuit photovoltages at greater photon energy (E_{Ph}) excitation (Figure 1e). The observed photocurrent increases nearly linearly with bias from −0.1 to 0.1 V, reflecting a decrease in E_B with increasing forward bias. The maximum V_{HC_OC} is thus the photon energy minus the barrier height, assuming no back-electron drift current (I_{drift}). The hot-hole photovoltage (V_{HC_OC}) can be represented as follows:

$$V_{HC\_OC} = (E_{ph} - E_B)(1 - I_{drift}/I_{HC})/e \quad (1)$$

To determine the I_{HC} quantum efficiency, the number of absorbed photons is controlled using PtA/hv, where P is the incident power, t denotes the time, A is the absorption percentage of light, and hv is the photon energy. Figure 1e presents the I-V curves of the device under different illumination wavelengths, with an equivalent absorbed photon density of 9.08×10^9 cm^{-2} s^{-1}. At shorter wavelengths, carriers are excited to higher energy levels, resulting in hot carriers with greater excess energies. This increases the likelihood of overcoming the VBM barrier and facilitating transport to MoS_2 for photocurrent generation. Under 375 nm illumination, the internal quantum efficiency (IQE = EQE/A) and EQE of the hot-carrier photocurrent at zero bias are 69.5% and 35.4%, respectively (Figure 1f), significantly higher than values reported in previous studies using conventional nanomaterials.[15] In addition, control measurements were performed on devices using quasi-2D perovskite and MoS_2 layers alone as active materials; however, no positive photocurrent was observed under similar light illumination across various pump intensities and wavelengths (Figure S7, Supporting Information, for details). Additionally, to further

verify our findings, another perovskite/MoS_2 heterostructure device is fabricated and tested (see Figure S8 in Supporting Information). The EQE and IQE values under illumination at 520 nm, 450 nm, and 375 nm are consistent with the results obtained in Fig. 2f.

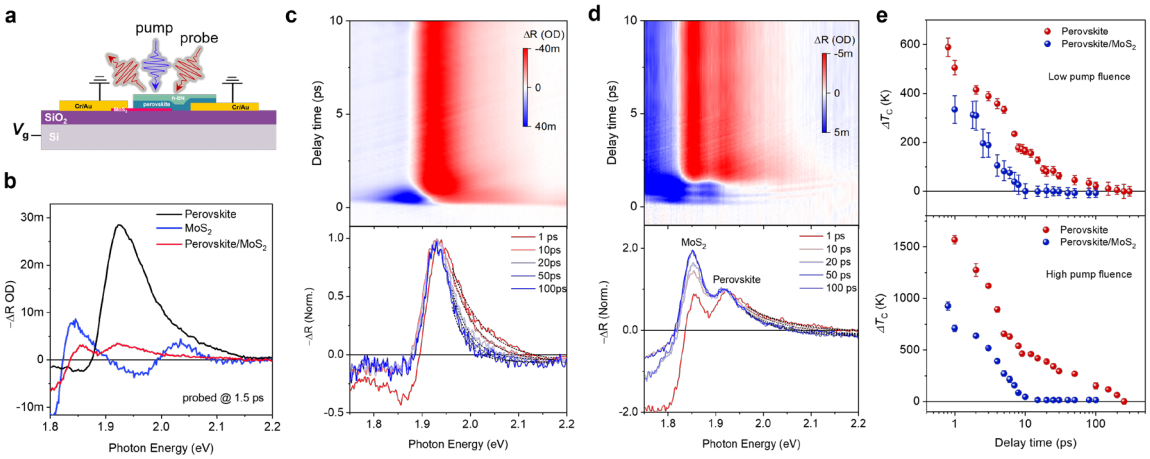

Figure 3. Evidence of hot-carrier extraction in the device. a) Schematic of the operando transient reflection measurements on the device. b) Transient reflection (TR) spectra of 2D $(BA)_2(MA)_2Pb_3I_{10}$ perovskite, MoS_2 and the perovskite/MoS_2 heterostructure with pump photon energy of 3.1 eV at 1.5 ps. Pseudo color plot of time-dependent TR spectra (top) and normalized TR spectra (bottom) of c) $(BA)_2(MA)_2Pb_3I_{10}$ perovskite and d) the heterostructure at various delay times with pump photon energy of 3.1 eV. e) Extracted hot-carrier temperature versus delay time of perovskite (n = 3) and perovskite/MoS_2 with excitation fluence of ~ 1.02 × 10^{10} cm^{-2} per pulse (top) and 5.09 × 10^{10} cm^{-2} per pulse (bottom).

2.3. Verification of hot-hole extraction using transient reflection spectroscopy

To further validate the generation of hot-carrier photocurrent, transient reflection (TR) spectroscopy was applied to the device to monitor the dynamics of HC generation and extraction in the device (as shown schematically in **Figure 3**a, with additional details in Figure S9, Supporting Information). The TR spectra (ΔR), which are approximately proportional to the photoexcited carrier density when values are on the order of 10^{-3},[43] reveal several bleaching peaks ($-\Delta R > 0$) caused by state filling from photoexcited carriers (Figure 3b). The heterostructure exhibits two bleaching peaks at ~1.95 eV and ~1.85 eV, corresponding to the band edge of the perovskite and the A exciton of MoS_2, respectively. Notably, there is a pronounced high-energy tail above the band edge in the perovskite,

indicating the distribution of hot carriers, which gradually decays over 100 ps, signifying the hot-carrier cooling process (Figure 3c). In contrast, the normalized TA spectra of the pure MoS_2 control sample show little variation across different delay times (Figure S10, Supporting Information), suggesting negligible HC distribution above the band edge within the temporal resolution. The temperatures (T_c) of the equilibrium HCs in the perovskite and heterostructure can be extracted by fitting the high-energy tail with the Maxwell-Boltzmann function[19] (dashed lines in Figures 2c and 2d): $\exp[(E_f - E)/k_B T_c]$, where k_B is the Boltzmann constant and E_f is the quasi-Fermi energy. It is important to note that the HC temperature will gradually decay to the lattice temperature once cooling is complete. For the perovskite, T_c relaxes to reaches room temperature of 300 K, while the fitted T_c for the heterostructure sample stabilizes at a temperature (T_f) above room temperature (300 K) (see Figure S11, and hot-carrier energy loss rates in Figure S12 for details). The elevated T_f is attributed to the weak signal from the B exciton bleaching in MoS_2, which overlaps with the high-energy tail of the perovskite, resulting in a broader spectrum. To simplify the analysis, the carrier temperature difference ($\Delta T_c = T_c - T_f$), which reflects the HC temperature above the lattice temperature, is thus used to monitor the HC cooling and extraction process. Considering that the interband transition probability is the product of the optical matrix element and the density of states (DOS)[44], and our DFT calculations for $(BA)_2(MA)_3Pb_3I_{10}$ (n=3) perovskite reveal a larger DOS for hole states than for electron states (Figure S13, Supporting Information). This indicates that the high-energy tail in the TR spectrum should primarily due to hot holes.

Figure 3e (top) presents the extracted ΔT_s from TR spectra shown in Figures 3c and 3d, under an excitation fluence of ~ 1.02×10^{10} cm^{-2} per pulse, corresponding to a volume carrier density of ~ 2.55×10^{15} cm^{-3} per pulse using 3.1 eV photon energy. In the perovskite MQWs (n = 3), the initially generated HCs reach equilibrium within 1 ps, sustain 500 K at around 10 ps, and sustain above 300 K up to around 100 ps. This duration is significantly longer than that observed in the 3D bulk film and lower n homologues. This extended HC lifetime could be attributed to multiple split-off bands,[45-46] and reduced electron-phonon coupling in higher n perovskites.[47] Given the long-range nondiffusive hot-carrier transport

(i.e., quasiballistic transport for the initial hot carriers and nonequilibrium transport for the protected long-lived hot carriers), which can extend up to hundreds of nanometers[33], the hot holes in our quasi-2D perovskite of around 60-nm thick can thus effectively travel to the MoS_2 layer and reach the Au electrode, thereby generating HC photocurrent.

A reduction in the ΔT_c value, along with a shorter lifetime, is observed upon the addition of MoS_2 to the heterostructure (Figure 3e). Meanwhile, the relative TR signal of the A exciton in MoS_2 increases compared to the normalized TR peak intensity of perovskite as the delay time progresses (Figure 3d lower panel). Furthermore, due to the lack of available states in MoS_2 for hot electrons from the perovskite (Figure S13, Supporting Information), our calculated DFT results reveal the hot electrons are mainly localized on the perovskite surface, and there are few distributed hot-electron states in MoS_2, resulting in a low probability of hot-electron transfer. And also, at 0 V, the device exhibits a positive short-circuit current, indicating the hole transfer from the valence band of the perovskite to that of MoS_2. If electrons were transferring from the perovskite to MoS_2, we would expect the short-circuit current to be negative. These results provide more evidence of hot-hole extraction by MoS_2. Furthermore, at a higher excitation fluence of 5.09×10^{10} cm^{-2} per pulse (Figure 3e bottom), the HC temperature in perovskite increases and exhibits a longer lifetime due to the hot-phonon bottleneck effect,[17] resulting in a more significant reduction of ΔT_c. The increased extraction of hot holes to MoS_2 aligns with the enhanced hot-hole photocurrent observed in Figure 2c. Together, these ultrafast spectroscopy results and device data indicate that the MoS_2 layer functions as a “semi-selective” hot-carrier extraction contact, minimizing energy loss from hot-hole relaxation and effectively converting hot holes into photocurrent with increased electrochemical potential.

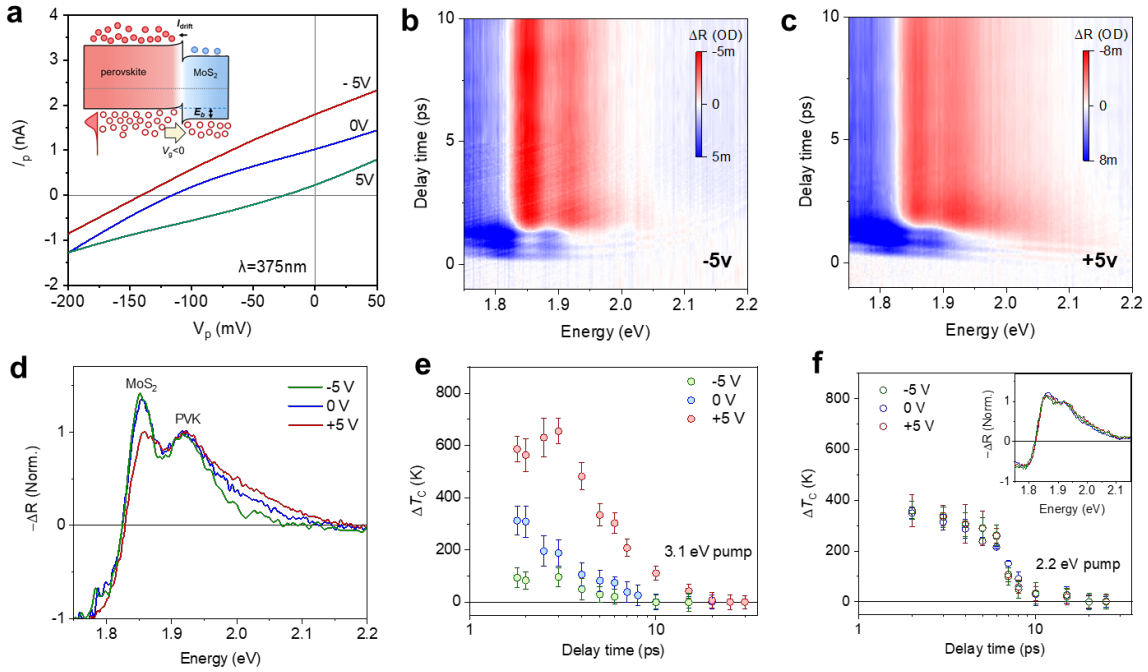

Figure 4 Gate-tunable hot-carrier photocurrent. a) I-V curves of the device under illumination at a wavelength of 375 nm (incident power of 2.26 mW/cm^2) without and with applied gate voltages of 5 V, -5 V. Inset: Schematic band alignment of the device under negative gate voltage for hot hole transport. Pseudo color plot of time-dependent TR spectra of the perovskite/MoS_2 heterostructure device with applied gate voltages of b) -5 V and c) 5 V under 3.10 eV fs laser photon excitaion. The excitation fluence is 1.02 × 10^{10} cm^{-2} per pulse. d) Normalized TR spectra of the heterostructure device. Time-dependent hot-carrier temperature difference (ΔT_C) as a function of time under e) 3.1 eV pump and f) under 2.2 eV pump at various gate voltages.

2.4. Gate-tunable hot-hole photocurrent generation

Since the hot-carrier extraction is influenced by the energy barrier E_B, reducing E_B could enhance both the hot-hole photocurrent and V_{HC_OC}. This effect could be observed and tuned by applying an external electric field, which shifts the Fermi level (E_F) of extraction layer due to carrier doping. To investigate this effect, the impact of back gate voltages (V_g) on hot-hole photocurrent is examined. A schematic representation of the band alignment for the device under different V_g is provided in Figure S14 of the Supporting Information. It is found that, at -5 V V_g, both the I_{HC} and V_{HC_OC} increase, whereas the opposite occurs at + 5V V_g (**Figure 4**a). To confirm these observations, TR measurements were performed on

the working device at different gate voltages. Figures 4b and 4c display the color plot TR spectra and normalized TR spectra, respectively. Under -5V V_g, the high-energy tail of perovskite decreases compared to that at 0V, while the MoS_2 TR signal strengthens. Conversely, at +5V V_g, the high-energy tail of the perovskite is enhanced, accompanied by a weakened MoS_2 TR signal. Figure 4e presents the extracted ΔT_c versus delay time with 3.1 eV photon excitation. Under -5V V_g, the initial ΔT_c drops from 500 K at 0 V to ~200 K, indicating improved hot-carrier extraction by MoS_2. The EQE and IQE of I_{ph} reach to ~ 61.9% and 121.5%, respectively (Figure 1f). An efficiency exceeding 100% implies that the hot holes may traverse the circuit more than once. In contrast, ΔT_c increases to ~900 K at +5V V_g. Additionally, under ~2.21 eV photoexcitation, where hot carriers have less excess energy, both the hot-carrier temperature and I-V curves remain relatively constant across positive and negative gate voltages (Figure 4d; see Figure S15 in the Supporting Information for details). This consistency further supports the presence of a hot-hole barrier, which can only be controlled by gate voltages. The inset of Figure 4a schematically illustrates how gate-voltage tuning of hot-hole extraction occurs in the heterostructure device, showing a reduced barrier E_b under negative V_g. When the external electric field (E-field) shifts the E_F of both the perovskite and MoS_2, a negative V_g with a positive electric field from perovskite to MoS_2 causes E_F shifts to drop to a lower energy level. Given the high carrier density and mobility in MoS_2, the E_F shift is more sensitive to the E-field than in the quasi-2D perovskite. A lower E_F leads to a reduced E_b, resulting in higher hot-hole photocurrent and voltage. These findings demonstrate the gate-tunable hot-hole photocurrent from perovskite to MoS_2, with an increased E_B expected under positive V_g. Moreover, a rapid conversion from photoinduced absorption (PIA) signal of perovskite to PB signal of MoS_2 is observed at 1.85 eV in perovskite/MoS_2 heterostructures and devices, which clearly indicates the hot-hole transfer occurring within 2 ps and is consistent with hot-carrier temperature results in Fig. 3-4 (detailed analysis is provided in Figure S16, Supporting Information).

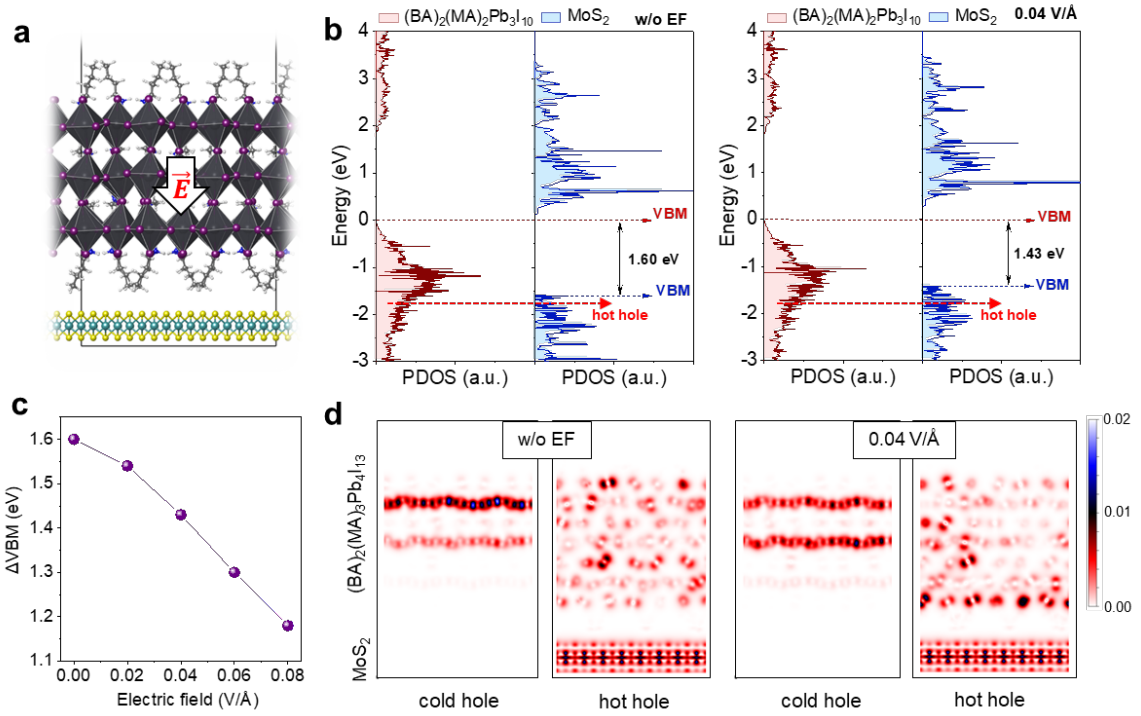

Figure 5. DFT calculations for hot-hole extraction. a) Sideview of optimized interfacial structures for $(BA)_2(MA)_2Pb_3I_{10}/MoS_2$ heterojunction. Projected density of states (PDOS) for the $(BA)_2(MA)_2Pb_3I_{10}/MoS_2$ heterojunction b) without and with an electric field of 0.04 V/Å. c) Energy difference of the valence band maximum (ΔVBM) between $(BA)_2(MA)_2Pb_3I_{10}$ and MoS_2 under the electric field. d) Charge density mapping (isovalue = 0.02 e/Å^2) of the hybrid state for hot and cold holes without and with an external electric field of 0.04 V/Å. The DFT calculations were performed at the GGA/PBE level.

2.5. DFT calculations for hot-hole extraction

To better understand the gate-tunable hot-hole photocurrent, DFT calculations were performed on the heterostructure. These calculations aimed to assess the effect of negative gate voltage in band alignment and the distribution of hot holes under an external electric field directed from p-type $(BA)_2(MA)_2Pb_3I_{10}$ perovskite MQWs toward the n-type MoS_2 (**Figure 5**a). As illustrated in Figure 5b and Figure S17 of the Supporting Information, the Fermi level of MoS_2 shifts closer to the valence band as the applied electric field increases. This shift reduces the VBM offset between MoS_2 and perovskite. Applying varying electric field to the heterostructure reveals that as the electric field increased, the energy barrier E_b decreased (Figure 5c). This indicates that the hot holes require less energy to overcome the

barrier, as depicted in the inset of Figure 4a. Additionally, Figure 5d provides charge density mapping for the hybrid state of cold holes (*i.e.*, excited holes at the band edge) and hot holes (*i.e.*, holes located 1.5 eV above the VBM of perovskite). In the absence of an electric field, cold holes are localized within the perovskite layer due to its lower VBM of perovskite (Figure 5b), while hot holes are delocalized across the heterostructure, showing their potential for transport to MoS_2. When an electric field is applied, the hot holes in perovskite shift closer to MoS_2, facilitating their extraction. In contrast, the electric field has little effect on the cold holes. These findings align with the electrical and transient reflection measurements obtained.

3. Conclusion

In conclusion, we demonstrated efficient hot-carrier photocurrent from halide perovskite by using perovskite $(BA)_2(MA)_2Pb_3I_{10}$ MQWs with ultralong-lived hot-carrier cooling. The hot holes in these perovskites can be efficiently extracted by a 2D MoS_2 layer. The EQE and IQE can reach up to 35.4% and 61.9%, significantly higher than previously reported values. The application of a gate electric field further enhances the hot-hole photocurrent and photovoltage by tuning the hot-carrier barrier height. Evidence of hot-carrier extraction and hot-carrier photocurrent enhancement was obtained through transient reflection spectroscopy measurements on the working devices, supported by DFT calculations. Moreover, other 2D TMDC semiconductors, such as WSe_2, which have a conduction band minimum higher than that of perovskite MQWs, can also serve as hot-electron extraction electrodes. When the perovskite is sandwiched between hot-electron and hot-hole electrodes, both types of carriers can be simultaneously extracted, leading to higher photocurrent and photovoltage. Our findings highlight the potential of perovskite MQWs as long-lived hot-carrier generators and 2D TMDC semiconductors as efficient hot-carrier extraction electrodes. These insights have significant implications for advancing low-power optoelectronic applications by effectively utilizing hot carriers.

4. Experimental section

Materials: Lead monoxide (PbO, 99.999%), methylammonium iodide (n-$CH_3(CH_2)_3NH_3I$, ≥99%) and *n*-butylammonium iodide (CH_3NH_3I, 98%) precursors were purchased from Sigma-Aldrich. Hydriodic acid (HI, 99.95%) and hypophosphorous acid (H_3PO_2, 50 wt.% in H_2O). Bulk MoS_2 was purchased from 2D Semiconductors USA.

Synthesis of $(BA)_2(MA)_2Pb_3I_{10}$ *single crystal:* $(BA)_2(MA)_2Pb_3I_{10}$ was prepared using the temperature-programmed method. PbO powder (2232 mg, 10 mmol) was dissolved in the mixture of 57% w/w aqueous HI (10 ml, 76 mmol) and 50% aqueous H_3PO_2 (1.7 ml, 15.5 mmol) with heating and constant magnetic stirring for 5 minutes. The boiling solution reaches a bright yellow color. The solid CH_3NH_3Cl (450 mg, 6.67 mmol) was subsequently added to the boiling solution, forming a black precipitate that was stirred to recover to a bright yellow solution. Then, a separate process in which n-$CH_3CH_2NH_2$ (327 ul, 3.33 mmol) was dissolved in 57% w/w HI (5 ml, 38 mmol) was conducted in an iced bath, resulting in a clear pale-yellow solution formation. Later, n-$CH_3(CH_2)_3NH_3I$ was added to the PbI_2 solution, heating and stirring until the black precipitate dissolved. The clear solution was left cooling to room temperature without stirring. Rectangular-shaped black plates began to crystallize during the cooling period, which ended after ~2 hours. The single crystal was collected by suction filtration and dried in drying oven.

Optical spectroscopy: For absorption, a fiber-coupled light source (EQ-77-fc, Energetiq) was utilized to generate broadband white light. Reflection and transmission measurements were performed on MoS_2, perovskite, and the perovskite/MoS_2 heterojunction. The white light was directly focused onto the sample and then captured by the spectrometer. The absorption spectra of MoS_2, perovskite, and the heterojunction were calculated using the equation A = 1 - R - T, where A denotes the absorption, R represents the reflection, and T signifies the transmission. TA spectroscopy was obtained using an amplified titanium: sapphire femtosecond laser (central wavelength 800 nm, pulse width 50 fs, repetition rate 1 kHz, Coherent Libra) equipped with an optical parametric amplifier (pump wavelength tunable from UV to IR, OPerA Solo) and a Helios pump-probe setup (probe wavelength

tunable from UV to NIR, Ultrafast Systems). Photoluminescence and Raman spectra were obtained using a Witec Confocal Raman System equipped with a laser source of 532 nm.

Device Fabrication: The Si and SiO_2/Si substrates (300 nm oxide layer) were cleaned sequentially using ultrasonic baths of acetone, isopropyl alcohol (IPA), and distilled water. A single metal electrode composed of Cr/Au (5 nm/15 nm) was then fabricated on the SiO_2/Si substrate through photolithography, thermal evaporation, and a lift-off technique in turn. Next, a few-layer MoS_2 was transferred onto the electrode and then annealed in an Ar atmosphere at 200 °C for 2 hours. A second metal electrode (Au, 50 nm) was deposited on a different Si substrate using the same process as the first electrode. This electrode was then transferred onto the MoS_2 layer via a wet transfer method using polyvinyl butyral (PVB), which was later dissolved in ethanol. The perovskite $(BA)_2(MA)_2Pb_3I_{10}$ multiple quantum wells were exfoliated onto a polymethyl methacrylate (PMMA) substrate and then transferred simultaneously onto both the first electrode and the MoS_2 layer using a 2D transfer system. Finally, a thin layer of hexagonal boron nitride (h-BN) was transferred onto the perovskite flake.

Device Measurements: The electrical tests of heterostructure devices were completed using a semiconductor analyzer (Keithley 4200-SCS) which is connected to the Lake Shore probe station in vacuum (10^{-6} Torr) under dark and illuminated environments and the reading bias is 0.5 V. The light source was provided by a fiber-coupled laser system with wavelengths of 375 nm, 450 nm, 520 nm, and 660 nm, respectively. The intensity of light was calibrated by a standard optical power meter (Newport 843-R with a PD300-UV optical power detector) before measurement.

Sample Characterization: The surface morphology was examined using a scanning probe microscope (Asylum MFP-3D Infinity). Cross-sectional TEM analysis was conducted with a transmission electron microscope (TEM, JEOL JEM-2100F), complemented by energy dispersive X-ray spectroscopy (EDS). X-ray diffraction (XRD) was carried out with a Bruker D8 Advance instrument, utilizing Cu Kα radiation (λ = 1.5418 Å) at 40 kV and 40 mA. Ultraviolet photoelectron spectroscopy (UPS) analysis was performed using a Thermo Scientific Nexsa instrument.

Computational Methods: Density functional theory (DFT) calculations were performed to optimize the crystal structures of $(BA)_2(MA)_2Pb_3I_{10}$ bulk, MoS_2 bulk, and $(BA)_2(MA)_2Pb_3I_{10}/MoS_2$ heterojunction using the projector augmented wave (PAW) method as implemented in VASP. The experimental crystal structures of $(BA)_2(MA)_2Pb_3I_{10}$ and MoS_2 at room temperature were used as starting points and were further optimized by relaxing atomic positions. The plane-wave cutoff energy was set to 450 eV for the bulk and 400 eV for the interfacial structures. The width of Gaussian smearing was set to 0.05 eV and the self-consistent field (SCF) energy convergence criterion was set to 1×10^{-5} eV. Γ-centered 4×4×4 and 6×6×1 *k*-meshes in the Brillouin zone were employed for bulk $(BA)_2(MA)_2Pb_3I_{10}$ and MoS_2, respectively. The heterojunction was built by placing 3×2 $(BA)_2(MA)_2Pb_3I_{10}$ (100) supercell on top of 8×3 MoS_2 (100) supercell, ensuing minimal lattice mismatch. The heterojunction was separated by a vacuum layer (~20 Å) to prevent spurious interlayer interactions. The heterojunction structure was further optimized under different external electric fields (0 to 0.08 V/Å) until the total force on each atom was less than 0.015 eV/Å.

Supporting Information

Supporting Information is available from the Wiley Online Library or from the author.

Acknowledgements

Dr. C. Wang and Dr. Q. Wei contribute equally to this work. This work was supported by Research Grant Council of Hong Kong (Project No. 25301522, 15301323, 15300824, C1055-23G, C5067-23G), Hong Kong Innovation and Technology Fund (ITS/064/22), National Natural Science Foundation of China (22373081), the Shenzhen Science, Technology and Innovation Commission (JCYJ20210324131806018) and Department of Science and Technology of Guangdong Province (2024A1515011261).

Conflict of Interest

The authors declare no conflict of interest.

Data availability. The experimental data that support the findings of this study are available from the corresponding author upon reasonable request.

Received: ((will be filled in by the editorial staff))
Revised: ((will be filled in by the editorial staff))
Published online: ((will be filled in by the editorial staff))

References

[1] W. Shockley, H. J. Queisser, *J Appl Phys* **1961**, 32, 510.
[2] Hamidreza Esmaielpour, Kyle R. Dorman, David K. Ferry, Tetsuya D. Mishima, Michael B. Santos, V. R. Whiteside, I. R. Sellers, *Nat Energy* **2020**, 5, 336.
[3] A. J. Nozik, *Nat Energy* **2018**, 3, 170.
[4] S. D. Stranks, H. J. Snaith, *Nat Nanotechnol* **2015**, 10, 391.
[5] U. Erkilic, P. Solis-Fernandez, H. G. Ji, K. Shinokita, Y. C. Lin, M. Maruyama, K. Suenaga, S. Okada, K. Matsuda, H. Ago, *ACS Appl Mater Interfaces* **2019**, 11, 40503.
[6] R. T. Ross, A. J. Nozik, *J Appl Phys* **1982**, 53, 3813.
[7] J. S. Kim, M. D. Tran, S. T. Kim, D. Yoo, S. H. Oh, J. H. Kim, Y. H. Lee, *Nano Lett* **2021**, 21, 1976.
[8] Y. L. Yuzhong Chen, Yida Zhao, Hongzhi Zhou, Haiming Zhu, *Sci Adv* **2019**, 5, eaax9958.
[9] M. Freitag, T. Low, F. Xia, P. Avouris, *Nat Photonics* **2012**, 7, 53.
[10] M. D. Tran, S. G. Lee, S. Jeon, S. T. Kim, H. Kim, V. L. Nguyen, S. Adhikari, S. Woo, H. C. Park, Y. Kim, J. H. Kim, Y. H. Lee, *ACS Nano* **2020**, 14, 13905.
[11] C. Ng, J. J. Cadusch, S. Dligatch, A. Roberts, T. J. Davis, P. Mulvaney, D. E. Gomez, *ACS Nano* **2016**, 10, 4704.
[12] K. H. W. Ho, A. Shang, F. Shi, T. W. Lo, P. H. Yeung, Y. S. Yu, X. Zhang, K. y. Wong, D. Y. Lei, *Adv. Funct. Mater.* **2018**, 28.
[13] Y. Yu, K. D. Wijesekara, X. Xi, K. A. Willets, *ACS Nano* **2019**, 13, 3629.
[14] S. Y. Y. Okada, *2010 35th IEEE Photovoltaic Specialists Conference* **2010**.
[15] I. J. Chen, S. Limpert, W. Metaferia, C. Thelander, L. Samuelson, F. Capasso, A. M. Burke, H. Linke, *Nano Lett* **2020**, 20, 4064.
[16] M. Li, J. Fu, Q. Xu, T. C. Sum, *Adv Mater* **2019**, 31, e1802486.
[17] Y. Yang, D. P. Ostrowski, R. M. France, K. Zhu, J. van de Lagemaat, J. M. Luther, M. C. Beard, *Nat Photonics* **2015**, 10, 53.
[18] L. Wang, Z. Wang, H. Y. Wang, G. Grinblat, Y. L. Huang, D. Wang, X. H. Ye, X. B. Li, Q. Bao, A. S. Wee, S. A. Maier, Q. D. Chen, M. L. Zhong, C. W. Qiu, H. B. Sun, *Nat Commun* **2017**, 8, 13906.
[19] M. Li, S. Bhaumik, T. W. Goh, M. S. Kumar, N. Yantara, M. Gratzel, S. Mhaisalkar, N. Mathews, T. C. Sum, *Nat Commun* **2017**, 8, 14350.
[20] I. C. Smith, E. T. Hoke, D. Solis-Ibarra, M. D. McGehee, H. I. Karunadasa, *Angew Chem Int Ed Engl* **2014**, 53, 11232.
[21] S. A. Yuhang Liu, Linfeng Pan, Ryusuke Uchida, Neha Arora, Jovana V. Milić,, F. S. Alexander Hinderhofer, Alexander R. Uhl, Shaik M. Zakeeruddin,, M. I. D. Anders Hagfeldt, Michael Grätzel, *Sci Adv* **2019**, 5, eaaw2543.
[22] T. Niu, J. Lu, M.-C. Tang, D. Barrit, D.-M. Smilgies, Z. Yang, J. Li, Y. Fan, T. Luo, I. McCulloch, A. Amassian, S. Liu, K. Zhao, *Energ Environ Sci* **2018**, 11, 3358.
[23] A. M. K. S. Novoselov, A. Carvalho,, A. H. C. Neto, *Science* **2016**, 353, 6298.
[24] B. Saparov, D. B. Mitzi, *Chem Rev* **2016**, 116, 4558.
[25] F. Zhang, H. Lu, J. Tong, J. J. Berry, M. C. Beard, K. Zhu, *Energ Environ Sci* **2020**, 13, 1154.

[26] M. B. Price, J. Butkus, T. C. Jellicoe, A. Sadhanala, A. Briane, J. E. Halpert, K. Broch, J. M. Hodgkiss, R. H. Friend, F. Deschler, *Nat Commun* **2015**, 6, 8420.
[27] K. Chen, A. J. Barker, F. L. Morgan, J. E. Halpert, J. M. Hodgkiss, *J Phys Chem Lett* **2015**, 6, 153.
[28] M. Li, Q. Wei, S. K. Muduli, N. Yantara, Q. Xu, N. Mathews, S. G. Mhaisalkar, G. Xing, T. C. Sum, *Adv Mater* **2018**, 30, e1707235.
[29] C. C. Stoumpos, D. H. Cao, D. J. Clark, J. Young, J. M. Rondinelli, J. I. Jang, J. T. Hupp, M. G. Kanatzidis, *Chemistry of Materials* **2016**, 28, 2852.
[30] H. Tsai, W. Nie, J. C. Blancon, C. C. Stoumpos, R. Asadpour, B. Harutyunyan, A. J. Neukirch, R. Verduzco, J. J. Crochet, S. Tretiak, L. Pedesseau, J. Even, M. A. Alam, G. Gupta, J. Lou, P. M. Ajayan, M. J. Bedzyk, M. G. Kanatzidis, *Nature* **2016**, 536, 312.
[31] M. Rahil, R. M. Ansari, C. Prakash, S. S. Islam, A. Dixit, S. Ahmad, *Sci Rep* **2022**, 12, 2176.
[32] D. H. Cao, C. C. Stoumpos, O. K. Farha, J. T. Hupp, M. G. Kanatzidis, *J Am Chem Soc* **2015**, 137, 7843.
[33] Y. W. Zhi Guo, Mengjin Yang, Jordan Snaider, Kai Zhu, Libai Huang, *Science* **2017**, 356.
[34] R. Austin, Y. R. Farah, T. Sayer, B. M. Luther, A. Montoya-Castillo, A. T. Krummel, J. B. Sambur, *Proc Natl Acad Sci U S A* **2023**, 120, e2220333120.
[35] C. Trovatello, G. Piccinini, S. Forti, F. Fabbri, A. Rossi, S. De Silvestri, C. Coletti, G. Cerullo, S. Dal Conte, *npj 2D Mater Appl* **2022**, 6.
[36] K. K. Paul, J.-H. Kim, Y. H. Lee, *Nat Rev Phys* **2021**, 3, 178.
[37] H. Ying, X. Li, H. Wang, Y. Wang, X. Hu, J. Zhang, X. Zhang, Y. Shi, M. Xu, Q. Zhang, *Adv Opt Mater* **2020**, 8.
[38] A. Capasso, F. Matteocci, L. Najafi, M. Prato, J. Buha, L. Cinà, V. Pellegrini, A. D. Carlo, F. Bonaccorso, *Adv Energy Mater* **2016**, 6.
[39] A. S. R. Bati, M. Batmunkh, J. G. Shapter, *Adv Energy Mater* **2019**, 10.
[40] H. Lai, Z. Lu, Y. Lu, X. Yao, X. Xu, J. Chen, Y. Zhou, P. Liu, T. Shi, X. Wang, W. Xie, *Adv Mater* **2023**, 35, e2208664.
[41] C. C. Stoumpos, D. H. Cao, D. J. Clark, J. Young, J. M. Rondinelli, J. I. Jang, J. T. Hupp, M. G. Kanatzidis, *Chemistry of Materials* **2016**, 28, 2852.
[42] J. Hou, W. B. Li, H. Zhang, S. Sidhik, J. Fletcher, I. Metcalf, S. B. Anantharaman, X. T. Shuai, A. Mishra, J. C. Blancon, C. Katan, D. Jariwala, J. Even, M. G. Kanatzidis, A. D. Mohite, *Nat Synth* **2024**, 3.
[43] B. R. R Wang, N Kumar, MZ Bellus, HY Chiu, H Zhao, *Phys Rev B* **2012**, 86.
[44] A. J. Nozik, *Annual Review of Physical Chemistry* **2001**, 52, 193.
[45] I. Dursun, P. Maity, J. Yin, B. Turedi, A. A. Zhumekenov, K. J. Lee, O. F. Mohammed, O. M. Bakr, *Advanced Energy Materials* **2019**, 9.
[46] Q. Wei, H. Ren, J. Liu, Q. Liu, C. Wang, T. W. Lau, L. Zhou, T. Bian, Y. Zhou, P. Wang, Q. Lei, O. F. Mohammed, M. Li, J. Yin, *ACS Energy Letters* **2023**, 8, 4315.
[47] P. Maity, J. Yin, B. Cheng, J. H. He, O. M. Bakr, O. F. Mohammed, *J Phys Chem Lett* **2019**, 10, 5259.

Hot carrier devices with low-dimensional semiconductor heterostructures can enhance photon-to-current conversion beyond the Shockley-Queisser limit. This study presents a 2D van der Waals heterostructure device made of 2D perovskite quantum wells and few-layer MoS_2. The device shows efficient gate-tunable hot-hole photocurrent and high external quantum efficiency.

Authors

Chenhao Wang, Qi Wei, Hui Ren, Kin Long Wong, Qi Liu, Luwei Zhou, Pengzhi Wang, Songhua Cai, Jun Yin, Yingjie Li**

Title

Efficient gate-tunable hot-carrier photocurrent from perovskite multiple quantum wells

ToC figure